ACS NANO

www.acsnano.org

ARTICLE

CdSe/CdS/CdTe Core/Barrier/Crown Nanoplatelets: Synthesis, Optoelectronic Properties, and Multiphoton Fluorescence Upconversion

Ali Hossain Khan, Guillaume H. V. Bertrand, Ayelet Teitelboim, Chandra Sekhar M., Anatolii Polovitsyn, Rosaria Brescia, Josep Planelles, Juan Ignacio Climente,* Dan Oron,* and Iwan Moreels*

Cite This: *ACS Nano* 2020, 14, 4206–4215

Read Online

ACCESS | Metrics & More | Article Recommendations | Supporting Information

ABSTRACT: **Colloidal two-dimensional (2D) nanoplatelet heterostructures are particularly interesting as they combine strong confinement of excitons in 2D materials with a wide range of possible semiconductor junctions due to a template-free, solution-based growth. Here, we present the synthesis of a ternary 2D architecture consisting of a core of CdSe, laterally encapsulated by a type-I barrier of CdS, and finally a type-II outer layer of CdTe as so-called crown. The CdS acts as a tunneling barrier between CdSe- and CdTe-localized hole states, and through strain at the CdS/CdTe interface, it can induce a shallow electron barrier for CdTe-localized electrons as well. Consequently, next to an extended fluorescence lifetime, the barrier also yields emission from CdSe and CdTe direct transitions. The core/barrier/crown configuration further enables two-photon fluorescence upconversion and, due to a high nonlinear absorption cross section, even allows to upconvert three near-infrared photons into a single green photon. These results demonstrate the capability of 2D heterostructured nanoplatelets to combine weak and strong confinement regimes to engineer their optoelectronic properties.**

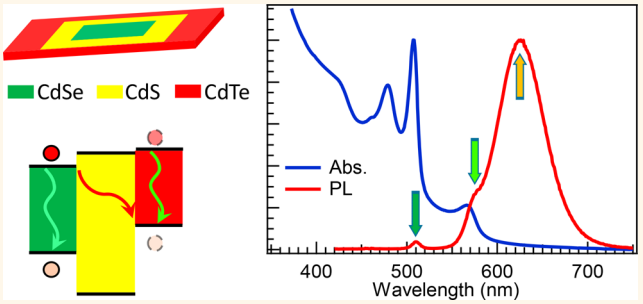

KEYWORDS: *nanoplatelets, ternary architecture, photoluminescence, k·p calculations, fluorescence upconversion*

Combining semiconductors at the nanoscale offers the possibility to tune electron and hole wave functions and their corresponding overlap, by choosing materials with the appropriate valence and conduction band offset. In colloidal nanocrystals, such wave function engineering has already resulted in type-I (*e.g.*, CdSe/ZnS)[1−3] and type-II (*e.g.*, CdTe/CdSe) quantum dots (QDs)[4] as well as intermediate systems such as CdSe/CdS QDs[5−7] where, in a regime of strong quantum confinement, the small conduction band offset leads to an electron delocalization over the entire heterostructure, while the hole remains confined to the CdSe core region (referred to as a quasi-type-II band offset).[8] Type-I, type-II, and quasi-type-II colloidal heteronanocrystals can be synthesized in a variety of shapes such as zero-dimensional dot-in-dot,[5] one-dimensional (1D) rod-in-rod,[9] two-dimensional (2D) core-crown nanocrystals,[10] or heterostructures with mixed dimensionality such as dot-in-rods[11] and dot-in-plates.[12] Heteronanocrystals offer a myriad of advantages, for instance, large absorption cross sections and sizable Stokes shifts in giant-shell QDs, efficient nonlinear emission due to reduced Auger recombination rates in quasi-type-II QDs, or polarized absorption and emission properties in anisotropic QDs.[6,13]

Among the different colloidal nanostructures, 2D nanoplatelets (NPLs) take a specific position. They combine strong and weak quantum confinement regimes, which yields on the one hand a band-edge emission peak at discrete wavelengths[14−16] and on the other hand a large band-edge oscillator strength and fast emission lifetime that scales with the area of the NPL.[17] The thickness can be controlled with monolayer precision, resulting in narrow emission line widths that are homogeneously broadened at room temperature.[16]

Received: November 18, 2019
Accepted: April 10, 2020
Published: April 10, 2020

https://dx.doi.org/10.1021/acsnano.9b09147
ACS Nano 2020, 14, 4206–4215

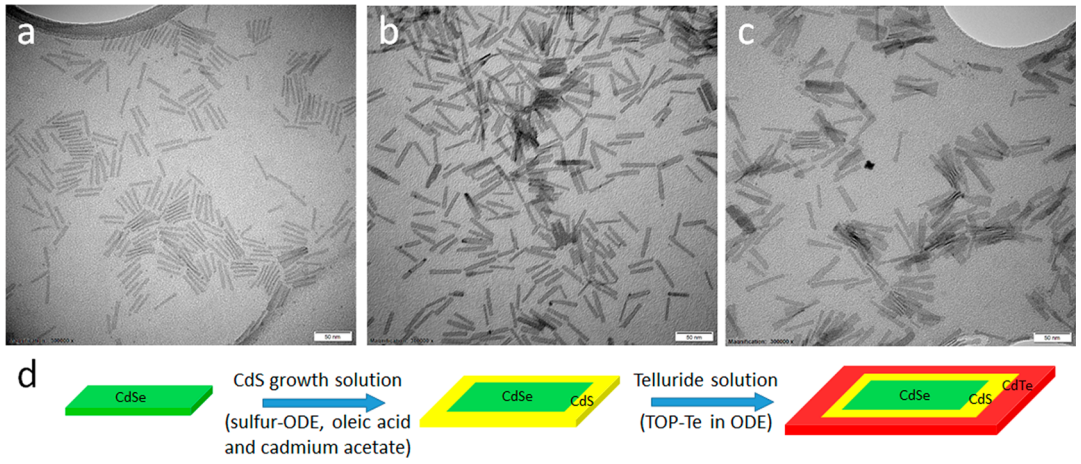

Figure 1. TEM images of (a) CdSe core, (b) CdSe/CdS core/barrier, and (c) CdSe/CdS/CdTe CBC NPLs (scale bars: 50 nm). (d) Schematic representation of the synthesis of CBC NPLs.

Due to the large NPL volume enabling weakly confined 2D excitons, they also exhibit a high two-photon absorption coefficient,[18] and the 2D shape leads to opportunities for self-assembly and ultrafast Förster energy transfer between NPLs.[19]

Recently, a variety of Cd-based NPL heterostructures have been synthesized, which can further shape the electron and hole wave functions.[20−24] In the case of concentric hetero-NPLs, type-I CdSe/ZnS NPLs yield fast photoluminescence (PL) lifetime,[25] in combination with a red shift of the band edge, while quasi-type-II CdSe/CdS core/shell NPLs combine an even larger red-shifted emission with a reduced PL decay rate.[26] One can also laterally extend the NPLs by growing a second material around the NPL edges. Interestingly, in this so-called core/crown configuration, the CdSe/CdS conduction band offset of *ca.* 300 meV is sufficient to retain the exciton confined to the core, yielding a type-I heterostructure,[10,26,27] highlighting the benefits of combining weak with strong confinement in 2D hetero NPLs. Type-II core/crown heterostructures, finally, have also been produced, in the form of CdSe/CdTe or CdS/ZnSe NPLs[28−30] as well as alloyed crown and multicrown ($CdSe/CdSe_{1-x}Te_x$, $CdSe/CdSe_{1-x}Te_x/CdS$) heterostructured NPLs.[30−33]

Considering the elements above, we created an even more elaborate ternary heterostructure that allows to further engineer emission properties and carrier dynamics in 2D NPLs. In this manuscript, we present the insertion of a type-I barrier in the CdSe/CdTe type-II junction, through synthesis of CdSe/CdS/CdTe core/barrier/crown (CBC) NPLs. Ternary architectures are known to increase the lifetime of charge-separated excitons or are engineered to control excited-state carrier dynamics[34] and have been developed as efficient dual-emitters.[34−36] In addition, they make excellent upconversion phosphors by creating hole- or electron-specific tunneling barriers. Our ternary architecture was chosen due to its potentially interesting band alignment, with a cascaded conduction band alignment permitting electron relaxation into the CdSe region, while the holes remain confined to either CdSe or CdTe due to the CdS valence band barrier. As a result, next to the extended exciton lifetime due to the charge-separated exciton, we also obtained two-photon and even three-photon upconversion fluorescence, the latter mediated by the efficient nonlinear absorption coefficient enabled in 2D NPLs as discussed by Scott *et al.*[18]

RESULT AND DISCUSSION

Based on our previous work, we first synthesized 4.5 monolayer (ML)-thick CdSe NPLs with controlled thickness and aspect ratio.[37] A typical sample is shown in Figure 1a and has lateral dimensions of 36 nm × 4.2 nm. Following Dubertret *et al.*,[10,28] we synthesized CdSe/CdS and CdSe/CdTe core/crown 2D NPLs as a reference for our CdSe/CdS/CdTe CBC NPLs. CdSe/CdS NPLs show the typical features of a type-I heterostructure, with the absence of a red shift of the emission peak after crown growth and a fast, monoexponential PL decay with a 3.3 ns lifetime (SI, Figure S1). CdSe/CdTe NPLs on the other hand display a strong band-edge red shift, with a PL emission at 637 nm and an extended PL lifetime of 124 ns (Figure S2), representative for type-II heterostructures. Based on these syntheses, we adopted a multistep, one-pot approach to create both CdS barrier and final CdTe crown. CdS and CdTe growth solutions were added consecutively, without intermediate isolation and purification of the CdSe/CdS NPLs. The 4.5 ML CdSe core NPLs were dispersed in 1-octadecene (ODE) along with cadmium propionate ($Cd(Prop)_2$). After degassing at 110 °C, the reaction temperature was increased to 235 °C, and the CdS growth solution (containing sulfur dissolved in ODE, oleic acid, and cadmium acetate dihydrate, $Cd(OAc)_2{\cdot}2H_2O$) was added dropwise for 2 min using a syringe pump, at a rate of 3 mL/h. After the injection of the CdS growth solution, the reaction was stirred for another 5 min at 235 °C. An aliquot was collected at that point to verify the CdS barrier thickness and to compare with the final CBC NPLs. As the CdS growth was executed under high cadmium excess (Cd:S ratio of 112:1), we only added additional Te (trioctylphosphine telluride dissolved in ODE) in the second step, again dropwise over the course of 3 min at a rate of 3 mL/h, followed by stirring for another 5 min. In Figure 1, we show transmission electron microscopy (TEM) images, depicting the result of a typical reaction, where we obtained CdSe/CdS NPLs with dimensions of 37 nm × 5.5 nm (Figure 1b) and finally, after CdTe crown growth, CBC NPLs of 52 nm × 9.1 nm (Figure 1c). A scheme depicting the synthesis route is shown in Figure 1d.

The CBC NPLs show the typical absorption features at 508 and 567 nm for the band-edge transitions of CdSe core and CdTe crown respectively (Figure 2a), while a CdS absorption onset can be discerned around 400 nm. The spectral position

https://dx.doi.org/10.1021/acsnano.9b09147
ACS Nano 2020, 14, 4206−4215

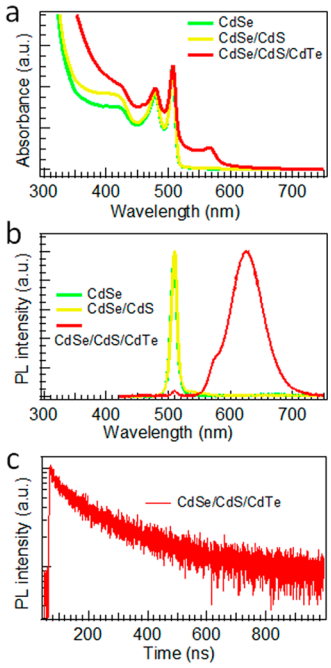

Figure 2. (a) Absorbance and (b) PL spectra of CdSe, CdSe/CdS, and CdSe/CdS/CdTe NPLs, respectively. (c) PL decay trace of the type-II transition monitored at 625 nm.

of the absorption peaks confirms that the 4.5 ML thickness does not change when growing the CdS and CdTe crown.[14] As the heavy hole−electron transition for a 4.5 ML CdTe NPLs was expected around 554 nm (Figure S2a),[14] the red-shifted value may be due to some inclusion of sulfur into the CdTe crown.[38,39] In the fluorescence spectrum, we measured three emission peaks (Figure 2b): two spectrally narrow signals at 510 and 575 nm and a broad band at 625 nm. These can be associated with the CdSe band-edge, the CdTe band-edge, and the indirect exciton transition, respectively. The first two are typically quenched in CdSe/CdTe NPLs (Figure S3).[28,30] Indeed, while in our CdSe/CdTe reference sample no more than 0.001% of the total spectrum consists of CdSe band-edge emission (Figure S3), in the sample shown in Figure 2, about 5% of the total area under the emission spectrum can be assigned to the combined CdSe and CdTe band-edge emission peaks (Figure S4). The indirect character of the emission at 625 nm is revealed by the extension of the PL decay time to 182 ns (Figure 2c). The lifetime of the direct transitions (from CdSe and CdTe) of CBC NPLs was also measured and compared with core-only and core/barrier NPLs (Figure S5). The PL decay curve was fitted with a triexponential function, from which the amplitude-weighted average lifetime was calculated. The average lifetime of the CdSe emission decreases from the core-only to the CdSe/CdS NPLs, and the value of 3.9 ns is similar to our CdSe/CdS reference sample (Figure S1). The CdSe PL lifetime is even slightly shorter in CBC NPLs, which we attribute to Förster resonance energy transfer from the CdSe core to the CdTe crown. The lifetime of the emission at 575 nm of CBC NPLs equals 76 ns, however, as the CdTe emission is weak and superposed on the type-II emission, we cannot disentangle both contributions.

PL excitation (PLE) spectroscopy supports that the emission peaks originate from a single heterostructure. First, when monitoring the emission at 510 nm for CdSe core-only, CdSe/CdS core/barrier, and CdSe/CdS/CdTe CBC NPLs, we observed that this emission peak can be excited *via* the CdSe absorption, and by comparing core-only CdSe with CdSe/CdS and CdSe/CdS/CdTe, a small increase from 420 nm onward indicates that the CdSe emission can be excited *via* the CdS absorption as well (Figure 3a). Second, the emission

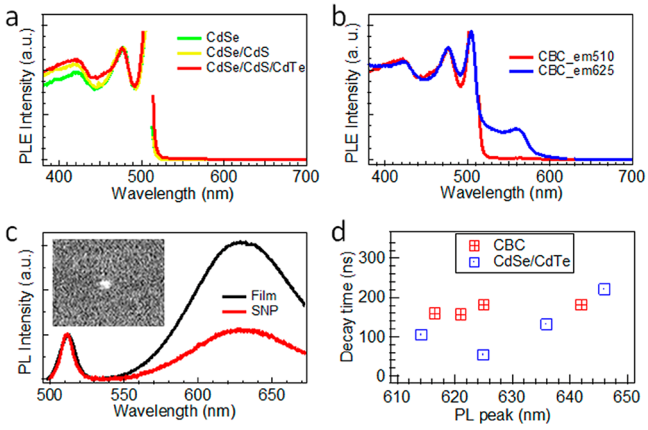

Figure 3. (a) PLE spectra, monitored at the CdSe emission at 510 nm for CdSe, CdSe/CdS, and CdSe/CdS/CdTe NPLs. (b) PLE spectra of the CdSe/CdS/CdTe CBC NPLs monitored at 510 nm and at the 625 nm indirect transition. (c) PL spectra of a CBC NPL thin film and of a single CBC NPL at room temperature (Batch5). Inset: Micrograph of the single CBC NPL. (d) Plot of the PL decay times against PL peak positions of the CBC samples (red squares) compared with the CdSe/CdTe reference samples (blue squares).

associated with the indirect transition in CBC NPLs, which we monitored at 625 nm, can be excited *via* the same absorption features that lead to the 510 nm CdSe band-edge emission in those heterostructures as well as the CdTe absorption, confirming that we indeed probe a single heterostructure (Figure 3b). We have also used another sample of CBC NPLs (Batch5) with more prominent CdS absorption (*i.e.*, a wider CdS barrier) and performed the PLE measurements as mentioned above (Figure S6). Here we more clearly observed the CdS absorption for all the PLE spectra, in addition to the CdSe and CdTe features, again supporting the CBC structure.

To further confirm the ternary heterostructures, we have performed elemental mapping by energy dispersive X-ray spectroscopy, coupled with high-angle annular dark-field scanning TEM imaging (HAADF STEM-EDS). However, while we clearly observed the Se, S, and Te signals in the EDS maps, we also noticed a significant electron-beam-induced degradation of the CBC NPLs (Figure S7), hindering a clear mapping on a single-particle level. We therefore resorted to single-NPL optical spectroscopy. Figure 3c shows a comparison of the PL spectrum of a single CBC NPL (SNP) with the corresponding close-packed thin film. Both the direct CdSe transition and the type-II emission of the CBC NPLs are clearly observed on a single NPL, with a decrease in full-width-at-half-maximum for the CdSe emission, from 13.6 nm in the thin film to about 10−11 nm for different single NPLs (Figure S8, Table S1). A single-particle micrograph of CBC is shown in the inset of Figure 3c. Note that we did not discern the CdTe emission in this sample (Figure 3a, Figure S6), however, this is explained by the relatively small CdTe crown (Table S2). Overall, about 2 in 10 NPLs did only show the type-II emission, indicative of NPLs with an incomplete CdS barrier,

https://dx.doi.org/10.1021/acsnano.9b09147
ACS Nano 2020, 14, 4206−4215

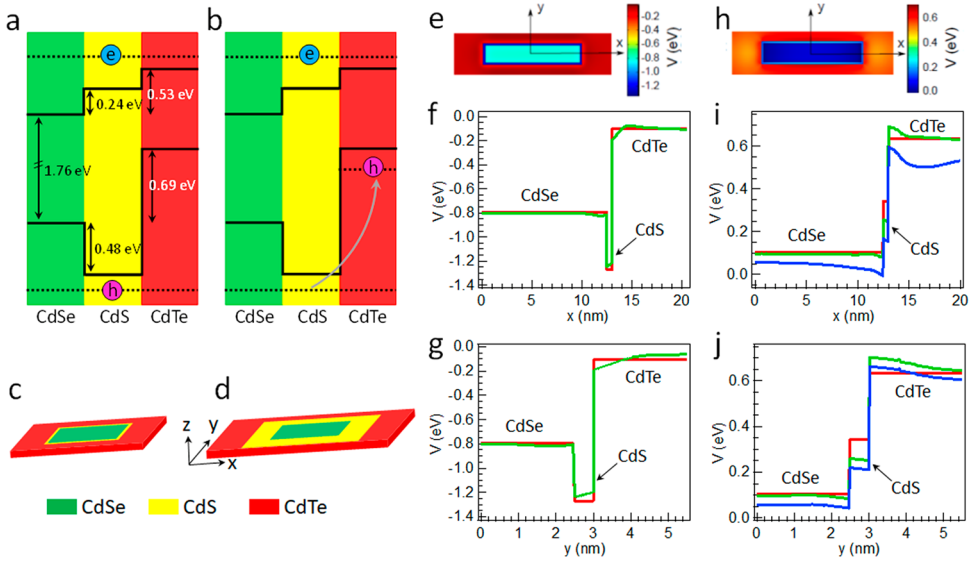

Figure 4. (a, b) Conduction and valence band alignment in the CBC heterostructure, considering unstrained band offsets. (a) A hot electron−hole pair is created. (b) The hole relaxes faster than the electron, conditioning the potential landscape that the hot electron sees at the moment of relaxation. (c, d) Schematic of the CBC NPLs under study, resembling Batch3 with a narrow CdS barrier (c) and Batch4 with a wider barrier (d). (e−g) Potential landscape seen by a photoexcited valence band hole for a narrow-barrier sample, with a 2D in-plane cross section (e) and 1D profiles along *x*- (f) and *y*- semi-axes (g), as depicted in (e). In the 1D plots, red and green lines show the potential excluding and including the influence of strain. The origin of energies is taken at the top of the CdTe band. (h−j) Same as (e−g) but for conduction band electrons. Blue lines in (i) and (j) panels show the potential including the Coulomb attraction exerted by the hole ground state localized in the CdTe crown. The origin of energies is taken at the bottom of the CdSe band.

and a minor fraction (2 out of 50 NPLs) only showed the CdSe emission, suggesting that they contain no CdTe crown. We did not observe particles that either show emission at other emission wavelengths than the ones above or at the wavelength of the CdTe NPL band-edge emission, leading to the conclusion that the synthesis does not lead to co-nucleation of separate nanocrystals and that the CdTe emission observed in the ensemble PL spectrum should also pertain to the CBC NPLs, as also demonstrated by the PLE spectroscopy.

Controlling the barrier and crown dimensions was achieved by injecting different amounts of Cd/S and Te growth solutions, always maintaining a fixed injection rate of 3 mL/h (Table S2 and Figure S9). In all cases, the reaction solution was stirred for 5 min before the injection of the Te solution. The resulting PL peak position of the type-II transition can be varied between 617 and 642 nm, similar to CdSe/CdTe NPLs without a CdS barrier (Figure S10). A measurement of the PL decay of the indirect transition in the different samples (Figure S10c) shows first that the PL decay time in CdSe/CdTe is dependent on the crown size. However, independent of these results, inclusion of a CdS barrier leads to an increased PL lifetime (Figure 3d and Table S3) when compared to CdSe/CdTe core/crown NPLs that emit at a similar wavelength. Note, for both CBC and CdSe/CdTe NPLs, we started from a CdSe core with similar dimensions. The data above are in line with the presence of a type-I CdS barrier for the hole, inserted between the CdSe core and the CdTe crown, leading to a reduced electron−hole overlap.

Hence, taking the transmission electron microscopy, which showed that we grow larger structures upon addition of CdS and then CdTe, the comparison of the ensemble and single-particle PL spectra, which confirmed that CdSe and broad peaks are reproduced on a single-particle level, the PLE spectra, which demonstrate that the CdTe emission can be excitated *via* the CdSe absorption, and the spectral and temporal tunability of the broad emission with crown dimensions, we can conclude that we synthesized CBC ternary heterostructured NPLs which exhibit both direct CdSe and CdTe emission as well as an indirect emission peak.

The general band structure, derived from bulk band offsets and depicted in Figure 4a and Figure 4b, shows how CdSe emission can be obtained when exciting the CdSe core directly, or when carriers relax in this region *via* excitation of the CdS barrier. To explain the CdTe emission, however, one needs to invoke a barrier for electron relaxation as well. This barrier may be caused by strain at the CdS/CdTe interface or be induced directly by the electron−hole Coulomb interactions and was investigated in further detail with *k*·*p* calculations. To this purpose, different CBC heterostructures were considered. We started by calculating the band structure of a CBC NPL with a narrow CdS barrier, comparable to experimental sample Batch3 (Figure 4c), and a CBC NPL with a wide CdS barrier, comparable to sample Batch4 (Figure 4d). The narrow-barrier NPL has a CdSe core of 25 nm × 5 nm, a CdS barrier of 1 nm × 1 nm, and a CdTe crown of 15 nm × 5 nm. The wide-barrier NPL has the same core and CdTe crown dimensions, but the CdS barrier is 15 nm × 5 nm. Both NPLs have a 4.5 ML thickness, assuming the CdSe lattice constant prior to strain relaxation. Electron and hole states are calculated with single-band *k*·*p* Hamiltonians, including dielectric mismatch with the organic medium and strain in the continuum elastic approximation (see SI for details on the calculation).

As we are interested in determining the origin of the CdTe emission, calculations are based on the consideration that the hot electron−hole pair relaxes, as shown in Figure 4. Initially, the hot electron and hot hole have high energy and barely feel the band offset profiles (Figure 4a). The hole relaxes faster than the electron, because the larger band offset and heavier mass (Table S4) provide a higher density of states, favoring phonon-mediated decay. This implies that the hot electron

https://dx.doi.org/10.1021/acsnano.9b09147
ACS Nano 2020, 14, 4206−4215

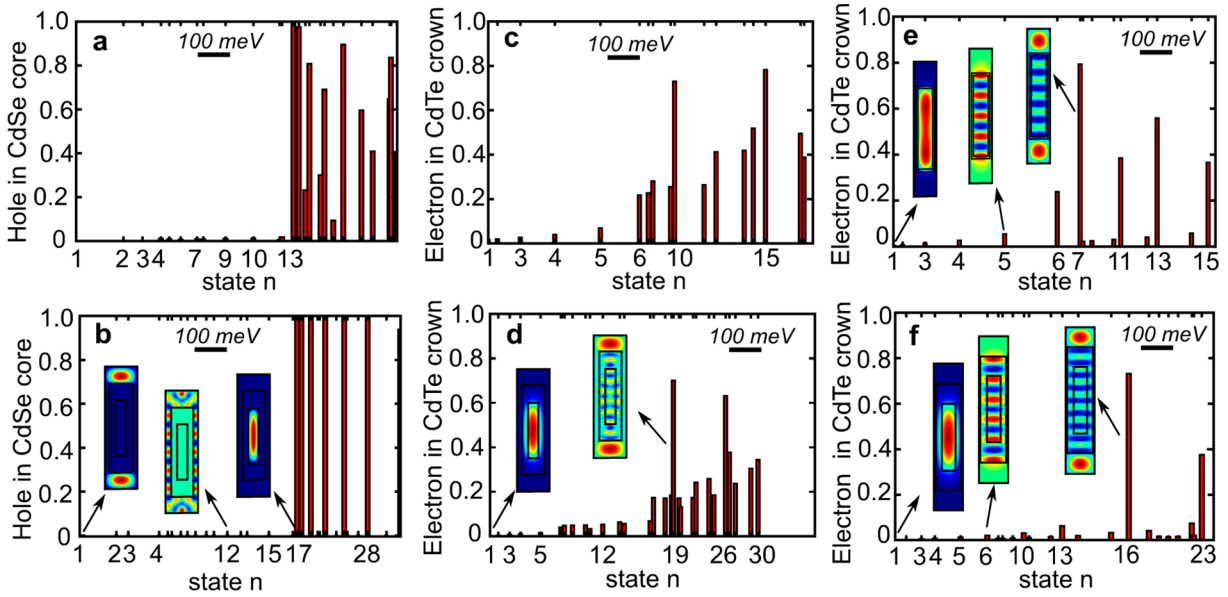

Figure 5. (a,b) Normalized fraction of the hole density that is localized in the CdSe core for different states with A_g symmetry, $|A_g, n\rangle$, for narrow- (a) and wide-barrier (b) NPLs. A 100 meV scale bar is included in the figures to illustrate the energy scale. The insets show a few representative envelope wave functions. The states are almost completely localized either in the CdTe crown or in the CdSe core. (c,d) The same plot for the density of electrons localized in the CdTe crown. Low-energy states remain confined to the CdSe core, while high-energy states delocalize over the entire NPL. (e,f) Normalized fraction of the electron density localized in the CdTe crown for different states, in a NPL with narrow (e) and wide (f) CdS barrier, and a CdTe crown of 15 nm × 1 nm (narrow along the *y*-direction). The insets show a few envelope wave functions. In (f), the $n = 16$ state shows strong localization in CdTe, while all other states at lower energy are almost completely localized in CdSe and CdS.

likely sees the Coulomb potential generated by the hole that has already relaxed to the CdTe crown band edge. The resulting potential landscape seen by valence band holes is shown in Figure 4f,g. The self-energy repulsion due to dielectric mismatch, V_{self}, shifts down the potential energy about 100 meV for all three materials, but it does not affect the relative band alignment. The main term affecting the band alignment is the unstrained band offset, V_{bo}, which turns CdS into a 0.48 eV high valence band barrier between the CdSe core and the CdTe crown (red line). Strain (Figure S11) somewhat modifies the overall potential (green line, and Figure S12 for calculations on the CBC NPL with wide CdS barrier), yet in any case, it yields only minor modifications as compared to V_{bo}.

Figure 4i,j shows the potential landscape seen by the electrons. In this case, we have a cascaded band alignment, again mainly set by V_{bo} (red lines in 1D plots). Here, strain does play a role. It raises (lowers) the potential in the CdSe (CdS) region, thus reducing the CdSe-CdS barrier from ∼0.25 eV to ∼0.20 eV. In addition, strain on the CdS/CdTe interface gives rise to a narrow potential well (barrier) on the CdS (CdTe) side (green line). In principle, this feature is capable of inducing localized states on the CdS barrier and/or confined states in the CdTe crown, which will now see a barrier up to 60 meV for narrow CdS and up to 80 meV for wide CdS. The inclusion of the Coulomb interaction with the hole ground state, localized in the CdTe crown, further enhances the depth of the barrier at the CdS/CdTe interface (Figure 4i,j, blue line), up to 90 meV for narrow CdS and up to 110 meV for wide CdS. The features are again shared qualitatively by wide and narrow barrier NPLs (Figure S12), although the effect is quantitatively stronger on the wide ones, because the CdTe side of the interface is slightly more compressed by strain (Figure S11).

These calculations already reveal that band bending due to strain and Coulomb interactions, which leads to local potential wells, can capture charges in a ground or high-energy state, with a wave function that can localize in either CdSe core or CdTe crown (see SI, section on $k\cdot p$ calculations for electron and hole wave function localization as a function of energy), yet they do not yield direct insight in the possibility for CdTe or CdSe band-edge emission. To this end, we also evaluated if the CdS barrier can influence the nonradiative decay of photoexcited electron−hole pairs and yield metastable states which can recombine radiatively in CdTe and CdSe before forming the indirect exciton. We assumed that the nonradiative decay is driven by phonons. The carrier-phonon coupling Hamiltonian, and hence the ensuing decay rate, is related to the interlevel energy spacing, which determines the density of available acoustic or optical phonon modes, and the carrier-phonon matrix element.[40] Figure 5 shows that the interlevel energy spacing is similar in both cases studied (narrow and wide barrier), therefore, we focused on the carrier-phonon matrix element. Within the dipolar approximation, the element is proportional to $|\langle f|\vec{r}|i\rangle|$, where i and f are the initial and final electron or hole states. Hence, the relaxation is determined by the wave function overlap between initial and final states.

Figure 5a,b represents the fraction of the hole charge density localized inside the CdSe core for narrow and wide barrier NPLs, respectively. We consider holes with A_g symmetry (within the D_{2h} group), $|A_g, n\rangle$, although the same observations hold for different symmetries. As expected, hole states localize either in the CdTe crown (with a nearly zero CdSe core density) or in the CdSe core (CdSe core density nearly one). Low-energy states mostly localize in the crown, while high-energy states can be either in the crown or in the core. Very little charge density is localized in the CdS barrier, and we found no states within the energetic window that we consider

https://dx.doi.org/10.1021/acsnano.9b09147
ACS Nano 2020, 14, 4206−4215

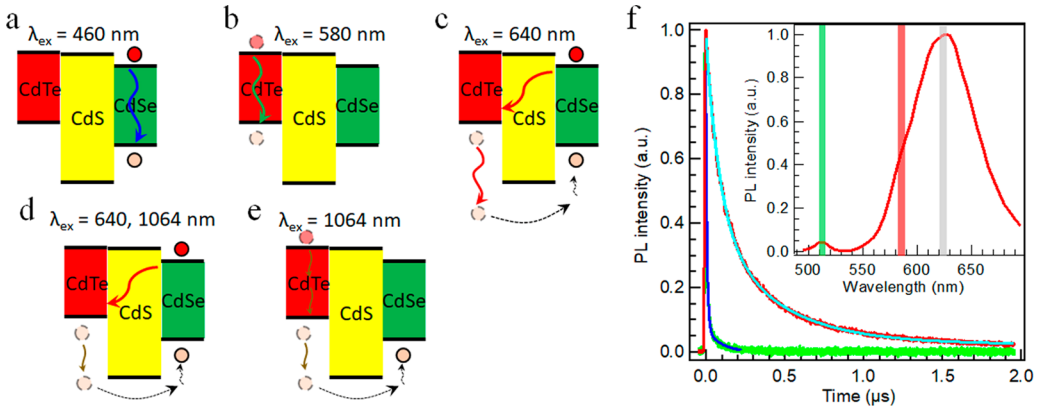

Figure 6. NPL band alignment and photoexcitation schemes. (a) Linear excitation of the CdSe core at λ_{ex} = 460 nm (exciting the CdTe crown and the indirect transition as well). (b) Linear excitation of the CdTe crown (and the indirect transition) using λ_{ex} = 580 nm. (c) Two-photon upconversion excitation of the CdSe core *via* the indirect transition, using λ_{ex} = 640 nm. (d) Pump−probe two-photon upconversion excitation of the CdSe core using a 640 nm excitation combined with a 1064 nm intraband absorption. (e) Three-photon upconversion excitation of the CdSe core, using two 1064 nm photons to excite the CdTe crown *via* two-photon absorption, followed by a 1064 nm intraband excitation. (f) NPL fluorescence decay (λ_{ex} = 460 nm, fluency 53 $\mu J/cm^2$) for the CdSe band-edge emission at 515 nm (green trace) and the indirect transition at 620 nm (red trace). The spectrum depicted in the inset is calculated from the time-integrated emission decay. The band-edge emissions for the different transitions (CdSe, CdTe peak, and the indirect transition) with the respective collection wavelength are marked in green, red, and gray, respectively.

(up to 0.8 eV above the ground state) delocalized over both core and crown. This is a consequence of the high and relatively wide type-I CdS barrier. Using a narrow barrier (Figure 5a), this effect is reduced, however, lowest-lying states still have either a CdSe-core or CdTe-crown localization, justifying a long-lived metastable hole state for the CdSe core.

Figure 5c,d shows the electron density in the CdTe crown. Because CdSe offers the lowest potential, low-energy states are mostly localized in the core and barrier (CdTe crown charge densities are nearly zero), but here, the localization in the crown increases gradually with state energy. A few states appear with dominant (over 70%) charge density in the crown, in spite of CdTe having high energy (Figure 4h−j). Such states partly arise from the small strain barrier on the CdS/CdTe interface. Nevertheless, the barrier is quite shallow, and, unlike in the case of holes, one finds electron states with partial localization in both CdSe core and CdTe crown even for a wide CdS barrier, and no long-lived electron state is derived.

However, in accordance with the experimental dimensions of the CBC NPLs, an important geometrical consideration still has to be considered: The presence of a CdTe crown with limited width (Table S2, Batch2). To this end, we calculated electron states for the CBC NPLs with a crown width that is reduced from 5 to 1 nm. The resulting electron density is plotted in Figure 5e,f. Interestingly, for a wide CdS barrier, the n = 16 state arises as an isolated state with large (almost 80%) localization in the CdTe crown, while neighboring states and lower-lying states have densities well below 10%. When compared to the wide crown (Figure 5d), where neighboring states reached densities of 20%, one notices that the narrow crown translates into a better separation of states localized in the core and states localized in the crown. These results are consistent with experimental data, where Batch2 NPLs for instance show a distinct emission from the CdTe crown with a relative weight of 6.7% (Figure S9). The role of the CdTe crown width can be interpreted as follows: Because the NPLs have in-plane anisotropy, electron states are more sensitive to the confinement in the narrow direction (width) than to that in the long direction (length). When growing wide CdTe crowns, electron states—even if low in energy—are prone to deposit part of their charge in the CdTe crown to minimize confinement energy. If the crown is narrow, this is no longer possible, and states with more definite localization (in CdSe core or in CdTe crown) are enabled.

Associated relaxation rates derived from $|\langle f|\vec{r}|i\rangle|$ are discussed in the Supporting Information (Figure S13) and support our conclusions. For valence band holes, the large (bulk) band-offset turns CdS into a high potential barrier, leading to hole states which are localized either in the CdSe core or in the CdTe crown. This implies that excited hole states localized in CdSe have slow phonon-mediated recombination rates toward the CdTe crown and explains the CdSe emission observed. For conduction band electrons, a moderate potential barrier forms at the CdS/CdTe interface, producing excited electron states that are largely (for 70−80%) localized in the CdTe crown. Electron localization either in CdSe or in CdTe is further favored by the presence of a narrow CdTe crown. Altogether, calculations yield metastable electron states mainly localized in CdTe, with relatively slow phonon decay rates toward CdSe, which are consistent with the CdTe emission observed.

Clearly, experimental data and $k\cdot p$ calculations support the formation of CdSe/CdS/CdTe CBC heterostructures with distinct type-II as well as CdSe and CdTe band-edge emission features. The ternary heterostructure combines an indirect ground state with direct excited-state transitions and should therefore allow for fluorescence upconversion. As reported previously, colloidal nanocrystals are particularly well suited for fluorescence upconversion,[41−43] in particular CdSe:Te/CdS/CdSe,[44] PbSe/CdSe/CdS,[45] and PbS/CdS-CdSe/ZnS[46] QDs have already demonstrated relatively high upconversion efficiencies (of the order of several percent) of near-infrared light. Here we excited sample Batch2 with 5 ns pulses at a repetition rate of 10 Hz, probing the CBC NPL transient fluorescence spectrum to investigate the upconversion process. Excitation wavelengths were selected in order to distinguish between linear and nonlinear excitation (Figure 6). For CBC NPLs, 460 nm is energetic enough to directly excite the CdSe region and obtain CdSe band-edge fluorescence in the single-

https://dx.doi.org/10.1021/acsnano.9b09147
ACS Nano 2020, 14, 4206−4215

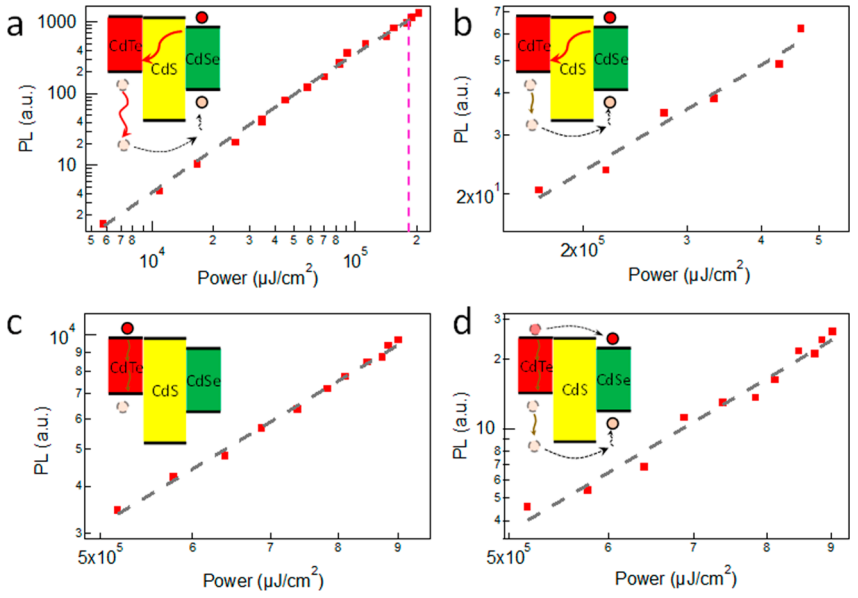

Figure 7. NPL fluorescence upconversion. (a) 640 nm upconversion excitation of the CdSe core. The data were fitted by a simplified Poisson distribution for the probability to absorb photon pairs plotted as the black dashed line. (b) Pump−probe upconversion excitation of the CdSe core using a 640 nm excitation with fixed excitation power, combined with a second pump at 1064 nm (yielding intraband absorption) with variable power. A fit of the power dependence $a{\cdot}P_{ex}^{b}$, with b = 1 is plotted as dashed line. (c) Two-photon excitation of the CdTe crown using 1064 nm excitation, monitored at 620 nm. A fit yields a b = 1.9 power dependence. (d) Fluorescence upconversion, monitored at 510 nm, created by three-photon excitation using λ_{ex} = 1064 nm. A fit of the power dependence yields b = 3.3.

photon regime. In contrast, using a pump wavelength of 580 or 640 nm, we can excite only the CdTe or the indirect transition, respectively, which requires two photons for detection of the excited-state CdSe emission. The transient decays at 515 and 620 nm, corresponding to the CdSe band edge and the indirect transition, respectively, are well fitted with a biexponential function (Figure 6f), with lifetimes of τ_1^{515} = 8.4 ns, τ_2^{515} = 100 ns and τ_1^{620} = 78 ns, τ_2^{620} = 390 ns, corroborating our time-resolved PL decay measurements.

First, a power series for different excitation wavelengths was acquired to check for the dependence of fluorescence intensity on excitation fluency and ensure that we excite the CBC NPLs below the saturation regime (Figure S14). Second, by exciting the sample with two 640 nm photons, we observed upconverted fluorescence at 515 nm arising from the CdSe core (Figure 7). The excitation proceeds through the formation of an indirect transition exciton, followed by either Auger recombination or intraband absorption to excite the hole into the CdSe region. The process was well fitted with a simplified Poisson distribution for the probability to absorb photon pairs:

$$FL_{UC} = \left(\frac{I^2}{2!} + 2{\cdot}\frac{I^3}{3!} + 3{\cdot}\frac{I^4}{4!} + 4{\cdot}\frac{I^5}{5!} + 5{\cdot}\frac{I^6}{6!} + \ldots\right){\cdot}e^{-I}{\cdot}\epsilon_{UC},\ I = \frac{I_{ex}}{I_{sat,UC}}$$

where FL_{UC} is the upconverted fluorescence intensity, and ϵ_{UC} < 1 is the upconversion efficiency, that is, the probability to heat up a hole and for it to be captured in the CdSe region before cooling. The saturation intensity was obtained as $I_{sat,UC510}^{ex_{640}}$ = 181 mJ/cm² and confirmed that we observed the upconverted fluorescence well below the saturation regime.

Using a second excitation photon at 640 nm implies that we cannot distinguish between hot hole creation *via* Auger recombination of two indirect excitons and *via* intraband absorption. We therefore employed a pump−probe excitation scheme (Figure 6d), which was comprised of an initial 640 nm excitation of the CBC NPLs at fixed excitation power (one-fifth of the saturation power), combined with a second excitation at 1064 nm that can only lead to heating of the CdTe valence band hole *via* intraband absorption. Figure 7b shows that the emission intensity at 510 nm, using the 640−1064 nm excitation scheme, fits a linear power dependence $a{\cdot}P_{ex}^{b}$ with b = 1, confirming that fluorescence upconversion occurs here *via* intraband absorption of the hole into a higher energy state and relaxation into the CdSe core.

In order to assess the upconversion efficiency ϵ_{UC}, a comparison can be made between the number of fluorescence counts per absorbed photon, at saturation intensity for two-photon ($I_{sat,UC513}^{ex_{640}}$) and linear excitation ($I_{sat,lin513}^{ex_{460}}$):

$$\epsilon_{UC} = \frac{FL_{sat,UC513}^{ex_{640}}}{FL_{sat,lin513}^{ex_{460}}}\frac{I_{sat,lin513}^{ex_{460}}OD_{460}}{I_{sat,UC513}^{ex_{640}}OD_{640}}$$

As both the upconversion ($FL_{sat,UC513}^{ex_{460}}$) and the linear ($FL_{sat,lin513}^{ex_{460}}$) fluorescence counts were measured at the same NPL concentration, the relation above yields the probability to excite the CdSe region, that is, the efficiency of the upconversion process. It gives a ratio of 0.014:1, which means that 36 absorbed NIR photon pairs are equivalent to one absorbed visible photon. Compared to other colloidal nanocrystals,[44−46] this efficiency is quite modest, likely due to the relatively large crown area of 71 nm² (compared to the overall NPL area of 338 nm²), and a possible remedy could be to further engineer the band structure to optimize relaxation of the hot hole toward the CdSe core.[46] On the other hand, the 2D shape offers a specific benefit. Due to the high nonlinear absorption coefficient,[18] not only two-photon but also three-photon upconversion is feasible. This was demonstrated by measuring the fluorescence upconversion using a 1064 nm excitation wavelength. As a result of two-photon absorption in the CdTe crown region around 532 nm, we first observed emission for the indirect transition at 620 nm, with a quadratic

https://dx.doi.org/10.1021/acsnano.9b09147
ACS Nano 2020, 14, 4206−4215

dependence on excitation fluency (Figure 7c, fitted power dependence with a slope of 1.9). Then, following intraband absorption through a third 1064 nm excitation photon, we then again obtained the CdSe core emission at 510 nm, here with a cubic fluency dependence (Figure 7d, fitted power dependence with a slope of 3.3).

CONCLUSION

We demonstrated the synthesis of a CdSe/CdS/CdTe 2D ternary heterostructure with an intermediate CdS barrier that separates emissive CdSe core and CdTe crown regions. This design allowed us to tune the indirect and direct transition energies and intensities as a function of the barrier and crown thickness. The theoretical results support the experimental data and reveal the formation of CdSe/CdS/CdTe CBC NPLs with distinct indirect as well as direct CdSe and CdTe band-edge transitions. While strong confinement applies to the vertical direction, 2D NPL charge carriers are typically only weakly confined in the lateral directions, which allowed us to obtain a type-I band offset at the CdSe/CdS interface, reducing the electron delocalization into the barrier and final CdTe crown. We obtained a heterostructure that exhibits efficient two-photon and, by the large nonlinear absorption coefficient induced by the 2D shape, even three-photon fluorescence upconversion. Our results demonstrate that shape-controlled colloidal nanocrystals offer an interesting pathway toward upconverting nanoparticles that can transform near-infrared to visible light, with potential applications in near-infrared upconversion-based photodetectors, solar cells, or biomedical imaging.[47−49]

EXPERIMENTAL METHODS

Chemicals. Cadmium nitrate tetrahydrate (99.997%), sodium myristate (99%), cadmium(II) acetate ($Cd(OAc)_2$; 99.995%), cadmium acetate dihydrate ($Cd(OAc)_2{\cdot}2H_2O$), octadecene (ODE; 90%), oleic acid (90%), trioctylphosphine (TOP; 90%), propionic acid (99.5%) methanol (99.9%), and hexane (95%) were purchased from Sigma-Aldrich. Cadmium oxide (99.999%) sulfur (S; 99.9%), selenium powder (Se; 99.99%), and tellurium (Te; 99.99%) were purchased from Strem Chemicals.

Synthesis of Type-I CdSe/CdS Core/Crown NPLs. Cadmium myristate ($Cd(Myr)_2$) and CdSe NPLs were synthesized according to a published procedure.[37] A 0.1 M solution of ODE-S in ODE was prepared by heating 32 mg of elemental sulfur in 10 mL of ODE. The CdS growth solution was prepared by mixing 2 mL of the 0.1 M ODE-S solution, 3 mL of ODE, 350 μL of oleic acid, and 400 mg of $Cd(OAc)_2{\cdot}2H_2O$. The resulting mixture is the sonicated for 2−3 h, forming a white gel. Next, in a 50 mL three neck round-bottom flask, a batch of CdSe NPLs in hexane was placed under argon flow to evaporate most of the hexane, the remaining part was then dissolved in 12 mL of ODE, and 100 mg of $Cd(propionate)_2$ was added to the reaction mixture. It was then stirred under vacuum at 110 °C for 20 min. After this degassing step, the mixture was placed under argon and heated to 235 °C. Using a syringe pump, the CdS growth solution was added dropwise (3 mL/h) in time varying from 2 to 12 min depending on the desired CdS thickness. The solution was then stirred at 235 °C for another 5 min and allowed to cool to room temperature. At 160 °C, 2 mL of oleic acid was added. The solution was diluted in 20 mL of hexane and then centrifuged at 6000 rpm for 10 min. The supernatant was discarded, and the precipitated NPLs were resuspended in hexane.

Synthesis of Type-II CdSe/CdTe Core/Crown NPLs. First, 128 mg of elemental Te was dissolved in 1 mL of TOP (1 M TOP-Te solution). The growth solution was prepared by mixing 75 μL of the 1 M TOP-Te with 1 mL of ODE right before injection. Next, in a 50 mL three neck round-bottom flask, a batch of CdSe NPLs in hexane was placed under argon flow to evaporate most of the hexane, the remaining part was then dissolved in 12 mL of ODE, and 100 mg of $Cd(propionate)_2$ was added to the reaction mixture. It was then stirred under vacuum at 110 °C for 20 min. After this degassing step, the mixture was placed under argon and heated to 235 °C. Using a syringe pump, the Te growth solution was added dropwise (3 mL/h). The addition was stopped when desired, and the solution was stirred at 235 °C for another 5 min and then cooled to room temperature. At 160 °C, 2 mL of oleic acid was added. The solution was purified as described above.

Synthesis of CdSe/CdS/CdTe CBC NPLs. For the preparation of the CdS and Te growth solutions, see previous sections. In a 50 mL three neck round-bottom flask, a batch of CdSe NPLs was placed under argon flow to evaporate most of the hexane, the remaining part was then dissolved in 12 mL of ODE, and 100 mg of $Cd(propionate)_2$ was added to the reaction mixture. It was then stirred under vacuum at 110 °C for 20 min. After this degassing step, the mixture was placed under argon and heated to 235 °C. Using a syringe pump, the CdS growth solution was added dropwise (3 mL/h) in time varying from 1 to 12 min. Afterward, the solution was stirred at 235 °C for another 5 min. Using a syringe pump, the Te growth solution was added dropwise (3 mL/h) in time varying from 2 to 16 min. The solution was stirred at 235 °C for another 5 min and then cooled to room temperature. At 160 °C, 2 mL of oleic acid was added. The solution purified as described above.

Transmission Electron Microscopy. A few drops of a dilute NPL suspension in hexane were dropped on a TEM grid (E. M. Sciences, Carbon film 300 mesh on copper) and inserted into a JEOL JEM-1011 electron microscope, operated at 100 kV. Bright-field TEM images were recorded, and the length and width of typically 50/75 NPLs were analyzed. To prepare the specimen for STEM-EDS analysis, 3 μL of sample (Batch3) was drop cast onto an ultrathin carbon/holey carbon-coated Cu grid and analyzed by an image-Cs-corrected JEOL JEM-2200FS TEM, operated at 200 kV, with in-column filter (Ω-type) and Bruker XFlash 5060 SDD system. The presented elemental maps are unprocessed, that is, obtained simply by integration of the Kα peaks of S and Se and Lα peaks of Te and Cd.

Absorbance and Time-Resolved Photoluminescence Spectroscopy. A dilute NPL suspension in hexane was added to a 3 mL quartz cuvette. Absorbance spectra were measured with a Cary300 Varian spectrometer. Fluorescence spectra were recorded using a Edinburgh instruments FLS920 spectrofluorometer. Time-resolved fluorescence decay traces were recorded either with a pulsed LED (331 nm, CdSe/CdS core/crown reference samples, CdSe/CdS/CdTe Batch3), or a pulsed laser (405 nm, CdSe/CdTe core/crown reference samples, CdSe/CdS/CdTe Batch1, Batch2, Batch4). PL decay measurements were performed in time-correlated single photon mode, selecting a region of typically 10 nm around the peak maximum. The pulse period was set to be 1−2 μs when monitoring the emission around 500 nm and 10−20 μs when measuring the decay around 600 nm, to ensure complete decay between the pulses.

Single Particle Spectroscopy. Single particle PL measurements were performed on a home-built microscope setup. The excitation wavelength (400 nm) was generated by frequency doubling a 800 nm laser (MaiTai, 80 MHz, 100 fs). The repetition rate was reduced to 1 MHz by a pulse selector (Spectra Physics, Model 3980). The excitation was focused onto the NPLs using a microscope objective (50×, NA = 0.80), and the PL from the NPLs was collected from the same objective. The pump fluence was around 20 $\mu J/cm^2$. The PL was recorded with an EMCCD (Prom EM HS, Princeton) camera attached to a spectrometer (Acton SP2300, Princeton). The sample was prepared by drop casting a dilute CBC solution onto precleaned glass cover slides.

Photoluminescence Upconversion Spectroscopy. A dilute solution of CBC nanocrystals dispersed in hexane was placed in 1 × 1 cm^2 quartz cuvette. The sample was excited by a 10 Hz, frequency tripled Nd:YAG Q-switched laser, pumping an optical parametric oscillator (Ekspla NT342/C/3/UVE), or by the residual laser pump at 1064 nm, all with a pulse duration of 5 ns. The laser excitation was focused on the sample, and the fluorescence was collected in the

https://dx.doi.org/10.1021/acsnano.9b09147
ACS Nano 2020, 14, 4206−4215

orthogonal direction using a 20× NA 0.4 objective, spectrally filtered using an appropriate dielectric filter to block the excitation laser and a monochromator (Acton SpectraPro2150i) and measured by a photomultiplier (Hamamatsu R10699). The photomultiplier transient output was measured by a 600 MHz digital oscilloscope (LeCroy Wavesurfer 62Xs). The pulse energy was measured by a pyroelectric sensor (PE9-C, Ophir Optronics). Transient spectra were collected around the fluorescence peak for a series of different excitation powers and subtracted for dark noise. The spectrum was calculated by integrating the transient PMT counts using the respective decay peak boundaries. For the 1064 nm fundamental laser line, a 594 nm long pass dielectric filter and an RG615 color glass were used as clean up filters. The beam area was estimated using a high resolution CCD camera (DCU223M, Thorlabs). The setup response function (RF) was measured to be 8 ns.

ASSOCIATED CONTENT

Supporting Information

The Supporting Information is available free of charge at https://pubs.acs.org/doi/10.1021/acsnano.9b09147.

Additional absorption, PL, and TEM data. Theoretical modeling and additional fluorescence upconversion data (PDF)

AUTHOR INFORMATION

Corresponding Authors

Iwan Moreels − *Department of Chemistry, Ghent University, 9000 Ghent, Belgium; Istituto Italiano di Tecnologia, 16163 Genova, Italy;* orcid.org/0000-0003-3998-7618; Email: iwan.moreels@ugent.be

Dan Oron − *Department of Physics of Complex Systems, Weizmann Institute of Science, Rehovot 7610001, Israel;* orcid.org/0000-0003-1582-8532; Email: dan.oron@weizmann.ac.il

Juan Ignacio Climente − *Departament de Química Física i Analítica, Universitat Jaume I, 12080 Castelló de la Plana, Spain;* orcid.org/0000-0001-6984-6424; Email: climente@qfa.uji.es

Authors

Ali Hossain Khan − *Department of Chemistry, Ghent University, 9000 Ghent, Belgium; Istituto Italiano di Tecnologia, 16163 Genova, Italy;* orcid.org/0000-0001-7155-0200

Guillaume H. V. Bertrand − *Istituto Italiano di Tecnologia, 16163 Genova, Italy*

Ayelet Teitelboim − *Department of Physics of Complex Systems, Weizmann Institute of Science, Rehovot 7610001, Israel*

Chandra Sekhar M. − *Department of Chemistry, Ghent University, 9000 Ghent, Belgium*

Anatolii Polovitsyn − *Istituto Italiano di Tecnologia, 16163 Genova, Italy*

Rosaria Brescia − *Istituto Italiano di Tecnologia, 16163 Genova, Italy;* orcid.org/0000-0003-0607-0627

Josep Planelles − *Departament de Química Física i Analítica, Universitat Jaume I, 12080 Castelló de la Plana, Spain*

Complete contact information is available at: https://pubs.acs.org/10.1021/acsnano.9b09147

Notes

The authors declare no competing financial interest.

ACKNOWLEDGMENTS

The present publication is realized with the support of the Ministero degli Affari Esteri e della Cooperazione Internazionale and the Ministry of Science, Technology and Space of the state of Israel (IONX-NC4SOL), and by the Crown Photonics Center of the Weizmann Institute of Science. This project has also received funding from the European Research Council (ERC) under the European Union's Horizon 2020 research and innovation program (grant agreement no. 714876 PHOCONA). J.C. and J.P. acknowledge the support from MINECO (project CTQ2017-83781-P) and UJI (project B2017-59). We also acknowledge the TEM facility of the Nematology Research Unit, member of the UGent TEM-Expertise center (life sciences).

REFERENCES

(1) Ghosh Chaudhuri, R.; Paria, S. Core/Shell Nanoparticles: Classes, Properties, Synthesis Mechanisms, Characterization, and Applications. *Chem. Rev.* **2012**, *112*, 2373−2433.

(2) Zhu, H.; Song, N.; Lian, T. Controlling Charge Separation and Recombination Rates in CdSe/ZnS Type I Core-Shell Quantum Dots by Shell Thicknesses. *J. Am. Chem. Soc.* **2010**, *132*, 15038−15045.

(3) Reiss, P.; Protière, M.; Li, L. Core/Shell Semiconductor Nanocrystals. *Small* **2009**, *5*, 154−168.

(4) Granados del Águila, A.; Groeneveld, E.; Maan, J. C.; de Mello Donegá, C.; Christianen, P. C. M. Effect of Electron−Hole Overlap and Exchange Interaction on Exciton Radiative Lifetimes of CdTe/CdSe Heteronanocrystals. *ACS Nano* **2016**, *10*, 4102−4110.

(5) Chen, O.; Zhao, J.; Chauhan, V. P.; Cui, J.; Wong, C.; Harris, D. K.; Wei, H.; Han, H.-S.; Fukumura, D.; Jain, R. K.; Bawendi, M. G. Compact High-Quality CdSe−CdS Core−Shell Nanocrystals with Narrow Emission Linewidths and Suppressed Blinking. *Nat. Mater.* **2013**, *12*, 445−451.

(6) García-Santamaría, F.; Chen, Y.; Vela, J.; Schaller, R. D.; Hollingsworth, J. A.; Klimov, V. I. Suppressed Auger Recombination in "Giant" Nanocrystals Boosts Optical Gain Performance. *Nano Lett.* **2009**, *9*, 3482−3488.

(7) Zhou, J.; Zhu, M.; Meng, R.; Qin, H.; Peng, X. Ideal CdSe/CdS Core/Shell Nanocrystals Enabled by Entropic Ligands and Their Core Size-, Shell Thickness-, and Ligand-Dependent Photoluminescence Properties. *J. Am. Chem. Soc.* **2017**, *139*, 16556−16567.

(8) Eshet, H.; Grünwald, M.; Rabani, E. The Electronic Structure of CdSe/CdS Core/Shell Seeded Nanorods: Type-I or Quasi-Type-II? *Nano Lett.* **2013**, *13*, 5880−5885.

(9) Christodoulou, S.; Rajadell, F.; Casu, A.; Vaccaro, G.; Grim, J. Q.; Genovese, A.; Manna, L.; Climente, J. I.; Meinardi, F.; Rainò, G.; Stöferle, T.; Mahrt, R. F.; Planelles, J.; Brovelli, S.; Moreels, I. Band Structure Engineering *via* Piezoelectric Fields in Strained Anisotropic CdSe/CdS Nanocrystals. *Nat. Commun.* **2015**, *6*, 7905.

(10) Tessier, M. D.; Spinicelli, P.; Dupont, D.; Patriarche, G.; Ithurria, S.; Dubertret, B. Efficient Exciton Concentrators Built from Colloidal Core/Crown CdSe/CdS Semiconductor Nanoplatelets. *Nano Lett.* **2014**, *14*, 207−213.

(11) Coropceanu, I.; Rossinelli, A.; Caram, J. R.; Freyria, F. S.; Bawendi, M. G. Slow-Injection Growth of Seeded CdSe/CdS Nanorods with Unity Fluorescence Quantum Yield and Complete Shell to Core Energy Transfer. *ACS Nano* **2016**, *10*, 3295−3301.

(12) Cassette, E.; Mahler, B.; Guigner, J.-M.; Patriarche, G.; Dubertret, B.; Pons, T. Colloidal CdSe/CdS Dot-In-Plate Nanocrystals with 2D-Polarized Emission. *ACS Nano* **2012**, *6*, 6741−6750.

(13) Pietryga, J. M.; Park, Y.-S.; Lim, J.; Fidler, A. F.; Bae, W. K.; Brovelli, S.; Klimov, V. I. Spectroscopic and Device Aspects of Nanocrystal Quantum Dots. *Chem. Rev.* **2016**, *116*, 10513−10622.

(14) Ithurria, S.; Tessier, M. D.; Mahler, B.; Lobo, R. P. S. M.; Dubertret, B.; Efros, A. L. Colloidal Nanoplatelets with Two-Dimensional Electronic Structure. *Nat. Mater.* **2011**, *10*, 936−941.

(15) Khan, A. H.; Brescia, R.; Polovitsyn, A.; Angeloni, I.; Martín-García, B.; Moreels, I. Near-Infrared Emitting Colloidal PbS Nanoplatelets: Lateral Size Control and Optical Spectroscopy. *Chem. Mater.* **2017**, *29*, 2883−2889.
(16) Christodoulou, S.; Climente, J. I.; Planelles, J.; Brescia, R.; Prato, M.; Martín-García, B.; Khan, A. H.; Moreels, I. Chloride-Induced Thickness Control in CdSe Nanoplatelets. *Nano Lett.* **2018**, *18*, 6248−6254.
(17) Naeem, A.; Masia, F.; Christodoulou, S.; Moreels, I.; Borri, P.; Langbein, W. Giant Exciton Oscillator Strength and Radiatively Limited Dephasing in Two-Dimensional Platelets. *Phys. Rev. B: Condens. Matter Mater. Phys.* **2015**, *91*, 121302.
(18) Scott, R.; Achtstein, A. W.; Prudnikau, A.; Antanovich, A.; Christodoulou, S.; Moreels, I.; Artemyev, M.; Woggon, U. Two Photon Absorption in II−VI Semiconductors: The Influence of Dimensionality and Size. *Nano Lett.* **2015**, *15*, 4985−4992.
(19) Rowland, C. E.; Fedin, I.; Zhang, H.; Gray, S. K.; Govorov, A. O.; Talapin, D. V.; Schaller, R. D. Picosecond Energy Transfer and Multiexciton Transfer Outpaces Auger Recombination in Binary CdSe Nanoplatelet Solids. *Nat. Mater.* **2015**, *14*, 484−489.
(20) Ithurria, S.; Talapin, D. V. Colloidal Atomic Layer Deposition (c-ALD) Using Self-Limiting Reactions at Nanocrystal Surface Coupled to Phase Transfer between Polar and Nonpolar Media. *J. Am. Chem. Soc.* **2012**, *134*, 18585−18590.
(21) Kelestemur, Y.; Guzelturk, B.; Erdem, O.; Olutas, M.; Gungor, K.; Demir, H. V. Platelet-In-Box Colloidal Quantum Wells: CdSe/CdS@CdS Core/Crown@Shell Heteronanoplatelets. *Adv. Funct. Mater.* **2016**, *26*, 3570−3579.
(22) Sun, H.; Buhro, W. E. Core−Shell Cadmium Telluride Quantum Platelets with Absorptions Spanning the Visible Spectrum. *ACS Nano* **2019**, *13*, 6982−6991.
(23) Altintas, Y.; Quliyeva, U.; Gungor, K.; Erdem, O.; Kelestemur, Y.; Mutlugun, E.; Kovalenko, M. V.; Demir, H. V. Highly Stable, Near-Unity Efficiency Atomically Flat Semiconductor Nanocrystals of CdSe/ZnS Hetero-Nanoplatelets Enabled by ZnS-Shell Hot-Injection Growth. *Small* **2019**, *15*, 1804854.
(24) Khan, A. H.; Pinchetti, V.; Tanghe, I.; Dang, Z.; Martín-García, B.; Hens, Z.; Van Thourhout, D.; Geiregat, P.; Brovelli, S.; Moreels, I. Tunable and Efficient Red to Near-Infrared Photoluminescence by Synergistic Exploitation of Core and Surface Silver Doping of CdSe Nanoplatelets. *Chem. Mater.* **2019**, *31*, 1450−1459.
(25) Polovitsyn, A.; Dang, Z.; Movilla, J. L.; Martín-García, B.; Khan, A. H.; Bertrand, G. H. V.; Brescia, R.; Moreels, I. Synthesis of Air-Stable CdSe/ZnS Core−Shell Nanoplatelets with Tunable Emission Wavelength. *Chem. Mater.* **2017**, *29*, 5671−5680.
(26) Lhuillier, E.; Pedetti, S.; Ithurria, S.; Nadal, B.; Heuclin, H.; Dubertret, B. Two-Dimensional Colloidal Metal Chalcogenides Semiconductors: Synthesis, Spectroscopy, and Applications. *Acc. Chem. Res.* **2015**, *48*, 22−30.
(27) Li, Q.; Wu, K.; Chen, J.; Chen, Z.; McBride, J. R.; Lian, T. Size-Independent Exciton Localization Efficiency in Colloidal CdSe/CdS Core/Crown Nanosheet Type-I Heterostructures. *ACS Nano* **2016**, *10*, 3843−3851.
(28) Pedetti, S.; Ithurria, S.; Heuclin, H.; Patriarche, G.; Dubertret, B. Type-II CdSe/CdTe Core/Crown Semiconductor Nanoplatelets. *J. Am. Chem. Soc.* **2014**, *136*, 16430−16438.
(29) Yadav, S.; Singh, A.; Sapra, S. Long-Lived Emission in Type-II CdS/ZnSe Core/Crown Nanoplatelet Heterostructures. *J. Phys. Chem. C* **2017**, *121*, 27241−27246.
(30) Dede, D.; Taghipour, N.; Quliyeva, U.; Sak, M.; Kelestemur, Y.; Gungor, K.; Demir, H. V. Highly Stable Multicrown Heterostructures of Type-II Nanoplatelets for Ultralow Threshold Optical Gain. *Chem. Mater.* **2019**, *31*, 1818−1826.
(31) Kelestemur, Y.; Guzelturk, B.; Erdem, O.; Olutas, M.; Erdem, T.; Usanmaz, C. F.; Gungor, K.; Demir, H. V. CdSe/CdSe1−xTex Core/Crown Heteronanoplatelets: Tuning the Excitonic Properties without Changing the Thickness. *J. Phys. Chem. C* **2017**, *121*, 4650−4658.
(32) Dufour, M.; Steinmetz, V.; Izquierdo, E.; Pons, T.; Lequeux, N.; Lhuillier, E.; Legrand, L.; Chamarro, M.; Barisien, T.; Ithurria, S. Engineering Bicolor Emission in 2D Core/Crown CdSe/CdSe1−XTex Nanoplatelet Heterostructures Using Band-Offset Tuning. *J. Phys. Chem. C* **2017**, *121*, 24816−24823.
(33) Liu, B.; Delikanli, S.; Gao, Y.; Dede, D.; Gungor, K.; Demir, H. V. Nanocrystal Light-Emitting Diodes Based on Type II Nanoplatelets. *Nano Energy* **2018**, *47*, 115−122.
(34) Galland, C.; Brovelli, S.; Bae, W. K.; Padilha, L. A.; Meinardi, F.; Klimov, V. I. Dynamic Hole Blockade Yields Two-Color Quantum and Classical Light from Dot-In-Bulk Nanocrystals. *Nano Lett.* **2013**, *13*, 321−328.
(35) Deutsch, Z.; Schwartz, O.; Tenne, R.; Popovitz-Biro, R.; Oron, D. Two-Color Antibunching from Band-Gap Engineered Colloidal Semiconductor Nanocrystals. *Nano Lett.* **2012**, *12*, 2948−2952.
(36) Soni, U.; Pal, A.; Singh, S.; Mittal, M.; Yadav, S.; Elangovan, R.; Sapra, S. Simultaneous Type-I/Type-II Emission from CdSe/CdS/ZnSe Nano-Heterostructures. *ACS Nano* **2014**, *8*, 113−123.
(37) Bertrand, G. H. V.; Polovitsyn, A.; Christodoulou, S.; Hossain Khan, A.; Moreels, I. Shape Control of Zincblende CdSe Nanoplatelets. *Chem. Commun.* **2016**, *52*, 11975−11978.
(38) Tenne, R.; Pedetti, S.; Kazes, M.; Ithurria, S.; Houben, L.; Nadal, B.; Oron, D.; Dubertret, B. From Dilute Isovalent Substitution to Alloying in CdSeTe Nanoplatelets. *Phys. Chem. Chem. Phys.* **2016**, *18*, 15295−15303.
(39) Wei, S.-H.; Zhang, S. B.; Zunger, A. First-Principles Calculation of Band Offsets, Optical Bowings, and Defects in CdS, CdSe, CdTe, and Their Alloys. *J. Appl. Phys.* **2000**, *87*, 1304−1311.
(40) Gantmakher, V.F.; Levinson, Y.B. *Carrier Scattering in Metals and Semiconductors*, 1st ed.; North Holland Physics Publishing: Amsterdam, 1987; Vol. *19*.
(41) Wu, M.; Congreve, D. N.; Wilson, M. W. B.; Jean, J.; Geva, N.; Welborn, M.; Van Voorhis, T.; Bulović, V.; Bawendi, M. G.; Baldo, M. A. Solid-State Infrared-To-Visible Upconversion Sensitized by Colloidal Nanocrystals. *Nat. Photonics* **2016**, *10*, 31−34.
(42) Wen, S.; Zhou, J.; Zheng, K.; Bednarkiewicz, A.; Liu, X.; Jin, D. Advances in Highly Doped Upconversion Nanoparticles. *Nat. Commun.* **2018**, *9*, 2415.
(43) Zheng, W.; Huang, P.; Gong, Z.; Tu, D.; Xu, J.; Zou, Q.; Li, R.; You, W.; Bünzli, J.-C. G.; Chen, X. Near-Infrared-Triggered Photon Upconversion Tuning in All-Inorganic Cesium Lead Halide Perovskite Quantum Dots. *Nat. Commun.* **2018**, *9*, 3462.
(44) Deutsch, Z.; Neeman, L.; Oron, D. Luminescence Upconversion in Colloidal Double Quantum Dots. *Nat. Nanotechnol.* **2013**, *8*, 649−653.
(45) Teitelboim, A.; Oron, D. Broadband Near-Infrared to Visible Upconversion in Quantum Dot−Quantum Well Heterostructures. *ACS Nano* **2016**, *10*, 446−452.
(46) Yang, G.; Meir, N.; Raanan, D.; Oron, D. Band Gap Engineering Improves the Efficiency of Double Quantum Dot Upconversion Nanocrystals. *Adv. Funct. Mater.* **2019**, *29*, 1900755.
(47) Kwon, S. J.; Lee, G. Y.; Jung, K.; Jang, H. S.; Park, J.-S.; Ju, H.; Han, I. K.; Ko, H. A Plasmonic Platform with Disordered Array of Metal Nanoparticles for Three-Order Enhanced Upconversion Luminescence and Highly Sensitive Near-Infrared Photodetector. *Adv. Mater.* **2016**, *28*, 7899−7909.
(48) Zhou, B.; Shi, B.; Jin, D.; Liu, X. Controlling Upconversion Nanocrystals for Emerging Applications. *Nat. Nanotechnol.* **2015**, *10*, 924−936.
(49) Wilhelm, S. Perspectives for Upconverting Nanoparticles. *ACS Nano* **2017**, *11*, 10644−10653.

https://dx.doi.org/10.1021/acsnano.9b09147
ACS Nano 2020, 14, 4206−4215